Fracture toughness of AlSi10Mg alloy produced by direct energy deposition with different crack plane orientations

Giorgia Lupi [a], João Teixeira Oliveira de Menezes [a], Filippo Belelli [a], Francesco Bruzzo [b], Elena López [b], Joerg Volpp [c], Enrique Mariano Castrodeza [a,*], Riccardo Casati [a,*]

[a] Department of Mechanical Engineering, Politecnico di Milano, Via G. La Masa 34, 20156 Milano MI, Italy
[b] Fraunhofer, Institut für Werkstoff und Strahltechnik, Winterbergstraße 28, 01277 Dresden, Germany
[c] Luleå University of Technology, Department of Engineering Sciences and Mathematics, SE-971 87 Luleå, Sweden

ABSTRACT

The fracture and tensile behaviors of the AlSi10Mg alloy processed by Direct Energy Deposition were investigated. Three-point bending fracture toughness and tensile specimens were tested at room temperature along different crack plane orientations and loading directions. Before being machined and tested, the printed samples were subjected to heat treatment at 300 °C for 2 h to relieve the residual stresses. Microstructural and fractographic analyses were performed to investigate the fracture mechanisms and the crack propagation paths for each crack orientation. Significant differences in the fracture toughness were observed among the crack plane orientations. Specimens with cracks oriented in the X-Y direction featured the highest fracture toughness values ($J_{Ic} = 11.96$ kJ/m^2), whereas the Z-Y crack orientation (perpendicular to the printing direction) performed the lowest fracture toughness values ($J_{Ic} = 8.91$ kJ/m^2). The anisotropy in fracture toughness is mainly related to a preferential crack propagation path along the melt pool boundaries. At melt pool boundaries, pores are preferentially placed, coarsening of the microstructure occurs and there is higher Si content, leading to that area being less ductile and less resistant to crack propagation.

1. Introduction

Additive Manufacturing (AM) has grown and changed over the past ten years due to its intrinsic advantages, such as flexibility, possibility to create complex shapes, and less waste of raw material [1]. Aluminum alloys are widely used in many sectors, including aerospace, automotive, and aircraft industries, due to their recyclability, high specific strength, good corrosion resistance, and good thermal conductivity. However, some of their physical properties, such as high reflectivity and high thermal conductivity, make laser processing Al alloys rather challenging [2,3]. Techniques such as Laser Powder Bed Fusion (LPBF) and Direct Energy Deposition (DED) are highly employed in 3D printing of aluminum alloys. DED refers to all processes where a focused beam, which can be a laser or electron beam, generates a melt pool into which feedstock material is fed to create a deposit. The feedstock can be in either powder or wire form. DED is performed using shielding gas or in an inert-gas filled build chamber to prevent the oxidation of the processed materials [4–6].

Among Al alloys, age-hardenable AlSi10Mg alloy is commonly used in AM thanks to its good processability, low susceptibility to hot cracking, good corrosion resistance, and mechanical properties. Few studies on the mechanical properties of specimens produced by DED have been published so far, and they mainly focus on hardness and tensile properties of the material. Lv et al. studied the tensile properties of an AlSi10Mg alloy fabricated by DED [7]. The results showed that the tensile strength of the as-built samples increased from 292 MPa to 342 MPa for the samples that were solution treated for a soaking time of 2 h and aged at 180 °C for 8 h. Mechanical properties of additively manufactured parts widely depend on the different post-printing heat treatments. Regarding AlSi10Mg, several heat treatment routes have been applied to reduce residual stresses and enhance mechanical properties. T6 temper, which consists in a solution treatment at ~470–530 °C followed by water quenching and artificial aging at ~160–220 °C, lead to a fine distribution of hardening phase, microstructure coarsening, and reduction of residual stresses [8]. Stress relief is usually performed at ~270–330 °C to mitigate the residual stresses and increase ductility and

---

* Corresponding authors.
E-mail addresses: enriquemariano.castrodeza@polimi.it (E.M. Castrodeza), riccardo.casati@polimi.it (R. Casati).

Table 1
List of used DED process parameters.

Laser power	2 kW
Laser spot diameter	1.6 mm
Scan speed fill	600 mm/min
Scan speed contour	450 mm/min
Powder flow	2.8 g/min
Carrier gas flow (Ar)	10 l/min
Shielding gas flow (Ar)	14 l/min
Track width	2.3 mm
Hatch distance	1.5 mm
Layer thickness	1.1 mm

toughness. T5 temper (i.e., direct artificial aging from the as built condition) is carried out at 160–220 °C to allow precipitation of hardening phases and preserving the fine solidification microstructure [9,10]. It allows achieving the maximum material hardness and strength, but low fracture toughness and elongation at fracture values [11].

The average microhardness and tensile strength of AlSi10Mg produced by DED are higher than those of the cast samples but lower than those of the samples processed by LPBF. This is because of the size of microstructural features (solidification cells/dendrites and eutectic constituents) generated by the different solidification rate in the three processes. In the AlSi10Mg alloy produced by DED, the finely dispersed Si particles enabled the achievement of improved static properties compared to those of the cast counterparts. However, crack tolerance along specific directions is usually moderate because of the weak interface between adjacent layers [12]. Indeed, at melt pool boundaries pores are preferentially placed, coarsening of the microstructure occurs and there is higher Si content, leading to that area being less ductile and less resistant to crack propagation[13,14].

The mechanical properties of as built DED samples are usually lower than those of their LPBF counterparts due to the finer microstructures that are formed in LPBF samples [15,16]. As an example, LPBF processed AlSi10Mg alloy shows higher yield and ultimate tensile strength than DED samples, due to high supersaturation degree of solid solution and very fine cell structure. However, the same material printed with DED, due to the coarser microstructural constituents, show higher ductility values [17]. Only a few papers have been published on the fracture behavior of DED materials [18–21]. The mechanical properties were found to depend on microstructure, processing parameters, and heat treatments. To the best of authors' knowledge, no studies on the fracture properties of AlSi10Mg processed by DED and their dependance on crack plane orientation are available in the open literature. Thus, this work focusses specifically on this topic, and it is an effort aimed to shed light on the microstructure-related mechanisms ruling the crack propagation in AlSi10Mg alloy produced by DED. Round tensile bars and three-point bending fracture toughness specimens were machined from bulk AlSi10Mg prismatic samples produced by DED and then stress relieved at 300 °C. The fracture specimens were notched having three different crack plane orientations. An in-depth characterization of the post-mortem material have been carried out by fractographic analyses and microstructural analyses, to correlate microstructural features, including melt pool boundaries (MPBs), pores, and microstructural constituents, to the crack path and final mechanical properties of the material.

2. Experimental

2.1. Material processing and heat treatment parameters

AlSi10Mg blocks with dimensions of 70 × 70 × 15 mm³ were printed

using laser and powder based DED using a DMG Mori Lasertec 65 system with a 4 kW diode laser source with wavelength range from 920 to 1080 nm. The DED process with process parameters listed in Table 1 was performed without the use of an inert atmosphere chamber resulting in higher porosity and surfaces oxidation [22].

The chemical composition of the powder is listed in Table 2. The particle size distribution of the powder was within the range 63–105 μm. After printing and before the machining operations, the samples were heat-treated at 300 °C for 2 h in inert atmosphere with oxygen content lower than 50 ppm to reduce the residual stresses. After heat-treatment, specimens for microstructural analysis, five tensile specimens and nine samples for fracture toughness tests were machined out from the block.

2.2. Mechanical testing

2.2.1. Tensile tests

Standard round tension test specimens oriented orthogonally to the building direction and identified as H (horizontal) were machined from heat-treated DED bars having a diameter of 4 mm and a gage-length of 15 mm. A schematic representation of the tensile specimens positioned on the build platform is shown in Fig. 1. Tensile tests were performed according to the ASTM E8/E8M-21 standard [23] using an MTS-Alliance RT/100 universal testing machine instrumented with a ± 100 kN load cell and an axial extensometer. Five tensile specimens were tested at room temperature under a constant crosshead speed of 1.0 mm/min.

2.2.2. Fracture toughness tests

SE(B) specimens for fracture toughness tests, with nominal dimensions of $W = 14.0$ mm and $B = 7.0$ mm, were machined out of heat-treated DED samples. The fracture tests were performed according to the ASTM E1820–20 standard [24] ($S = 56$ mm). The coordinate system defined by the ISO/ASTM 52921:2013 standard [25] for additive manufacturing terminology was applied. According to the referred standard, the Z axis was defined as the building direction, the X axis was defined as parallel to the front of the machine, and the Y axis was defined as perpendicular to the Z and X axes. Fig. 1 shows the orientation of the coordinate system used as a reference. Fracture specimens were identified as X-Y, X-Z, and Z-Y depending on the direction normal to the crack plane and crack plane orientation, following the nomenclature of the ASTM E1820–20 standard [24]. According to this document, the X-Y and X-Z specimens share the same crack plane, but crack extensions occur in perpendicular directions. The fatigue precracking procedure were conducted under force control, with a sinusoidal waveform at a frequency of 20 Hz and a load ratio (P_{min}/P_{max}) of 0.1.
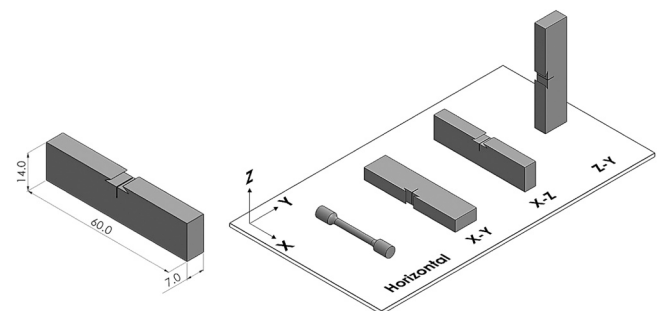
Fig. 1. Schematic representation of SE(B) and tensile specimens identified according to the coordinate system defined by ISO/ASTM 52921:2013 standard [25].
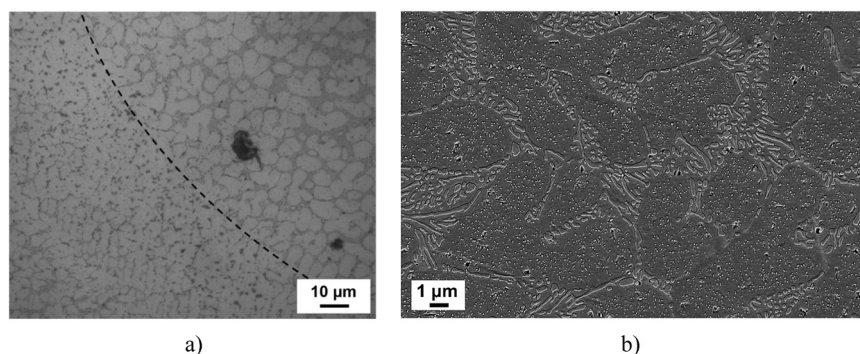
Table 2
Chemical composition (wt%) of the AlSi10Mg alloy powder.

Si	Mg	Fe	Cu	Mn	Ni	Zn	Pb	Sn	Ti	Al
10.00	0.35	0.55	0.05	0.45	0.05	0.10	0.05	0.05	0.15	Balance

a)   b)

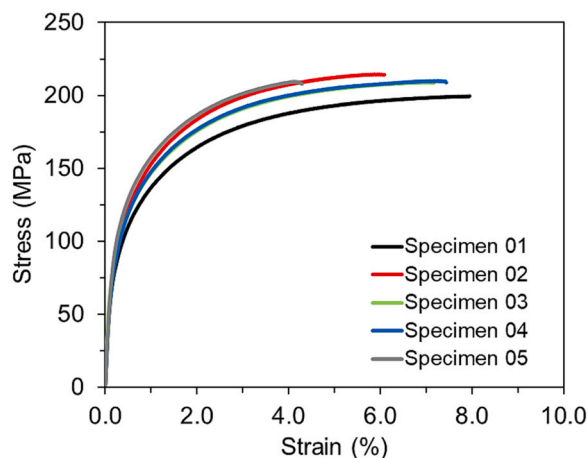**Fig. 2.** a) LOM micrograph of X-Z plane; b) SEM micrograph of X-Z plane.

Fig. 3. Engineering stress vs. strain records of stress relieved AlSi10Mg alloy.

Table 3
Main tensile properties of the stress relieved AlSi10Mg alloy.

Specimen	σ_{YS} [MPa]	σ_{UTS} [MPa]	σ_{YS}/σ_{UTS}	Elongation at fracture [%]
01	97.0	199.0	0.49	8.7
02	106.0	215.0	0.49	6.3
03	105.0	209.0	0.50	7.3
04	106.0	210.0	0.50	7.5
05	120.0	210.0	0.57	4.4
Mean	106.8 $\pm$ 7.4	208.6 $\pm$ 5.2	0.51 $\pm$ 0.03	6.8 $\pm$ 1.4

Like precracking, the fracture tests (three by orientation) were carried out at room temperature using an MTS Landmark servo-hydraulic testing machine instrumented with a $\pm$ 25 kN load cell and an MTS 632.02–20 fracture extensometer. The crack lengths were estimated using the unloading compliance method. After the tests, the SE(B) specimens were post-fatigued to mark the final crack extension precisely. The initial and final crack lengths were measured according to the 9-point average method described in the BS 7448–1:1991 standard [26].

2.3. Microstructural and fractographic analyses

The analysis of microstructure was performed by a light optical microscope (LOM) and a Field Emission Scanning Electron Microscope (FE-SEM) model Zeiss Sigma 500 equipped with energy dispersive X-ray analysis (EDX) and secondary electrons and backscattered electrons detectors. The fracture surfaces were analyzed with Zeiss EVO 50XVP Thermionic Scanning Electron Microscope (SEM) with the Oxford Inca Energy 200 X-ray microanalysis (EDS) detector. Samples for metallography were prepared following common grinding and polishing procedures. Chemical etching was performed by Keller's reagent to reveal the microstructural features. SE(B) specimens were cut orthogonally to the crack plane at half the specimen thickness, and the cut surfaces were grinded, polished, and etched using Keller's solution to investigate the crack path through the microstructure. The area fraction of pores was determined by analysis of LOM images of the cross sections of unetched samples. ImageJ software was used to obtain the porosity percentage.

3. Results

3.1. Microstructural analysis

Representative LOM image taken of a section parallel to the building direction (Z) is shown in Fig. 2-a. Fig. 2-a shows two melt pool regions characterized by different microstructures, i.e. the core with a dendritic microstructure surrounded by a fine Al-Si eutectic phase mixture and the Heat Affected Zone (HAZ) in which silicon particles are coarser and with spherical morphology. Fig. 2-b shows a higher magnification SEM image of the core region. In this image it is possible to appreciate the dendritic structure at the interdendritic eutectic constituent, and, within the primary α-Al phase, a dispersion of second phases. The average fraction of pores measured by image analysis for the samples is 1.95 $\pm$ 0.54%.

3.2. Tensile tests

The experimental tensile stress-strain records are shown in Fig. 3 and the tensile mechanical properties determined from these curves are listed in Table 3. As can be observed, an appreciable scatter in the tensile data was found. This behavior could be attributed to the presence of pores that can affect the mechanical properties of the material. In particular, the different distribution of these defects in the bulk samples can affect the consistency and repeatability of the test results [27].

3.3. Fracture tests

3.3.1. Load vs. CMOD records

The load vs. crack mouth opening displacement (P-CMOD) records for the SE(B) specimens tested in the X-Y, X-Z, and Z-Y crack orientations are shown from Fig. 4 to Fig. 6, respectively. A representative SEM image of the fracture surfaces is shown next to each plot. The unloading-reloading sequences are noticeable in the experimental records. In the fracture surface images, from the bottom to the top, the notch, fatigue pre-crack, stable crack growth (lighter region), and post-fatigue regions can be distinctly observed. The same regions are visible in the fracture surface, as shown below.

3.3.2. Crack growth resistance curves

From the P-CMOD records, the J-Integral values and the crack lengths were calculated for each specimen, and the correspondent J-Δa
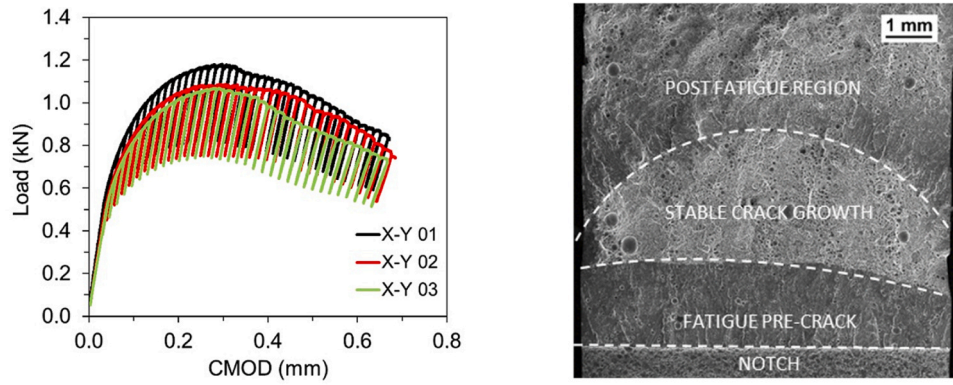
Fig. 4. P-CMOD records of the X-Y SE(B) specimens and representative SEM image of the fracture surface.
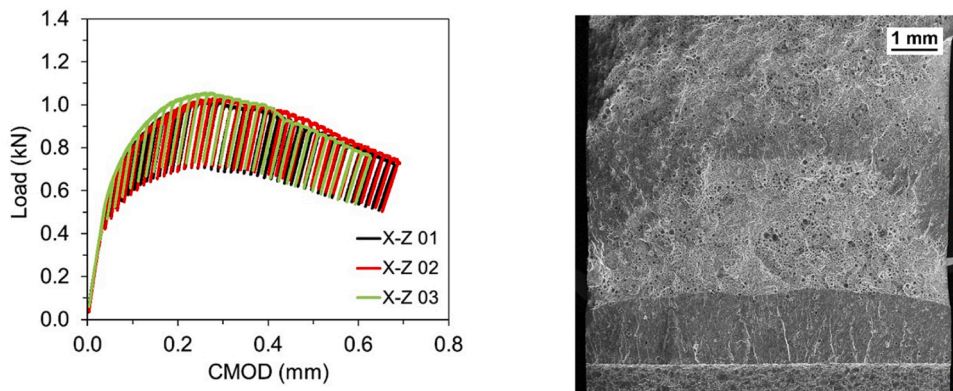

Fig. 5. P-CMOD records of the X-Z SE(B) specimens and representative SEM image of the fracture surface.
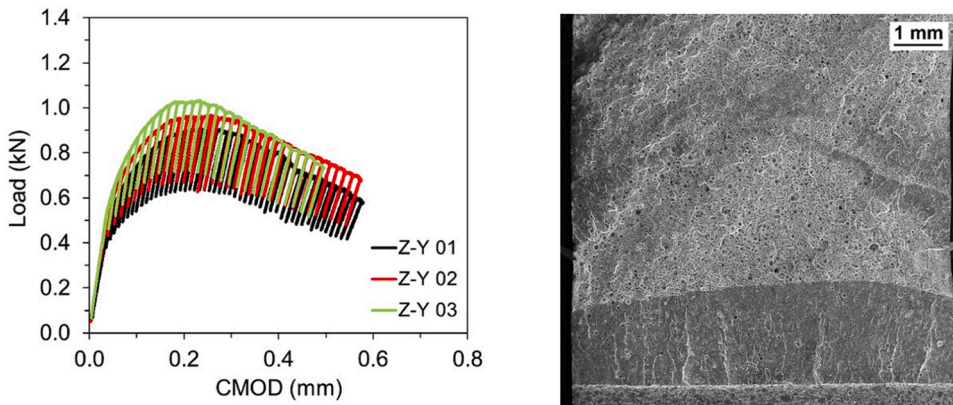

Fig. 6. P-CMOD records of the Z-Y SE(B) specimens and representative SEM image of the fracture surface.

pairs of points were obtained. Fig. 7 shows the J-Δa pairs for the specimens with cracks in the X-Y orientation, Fig. 8 for the X-Z orientation, and Fig. 9 for the Z-Y orientation. In addition, the blunting line, the 0.15 mm and 1.50 mm exclusion lines, and the 0.5 mm offset line for qualifying the data were also plotted. From these figures, it is also possible to observe the fitted crack growth resistance (J-R) curves according to the ASTM E1820–20b standard [24].

Fig. 10 shows all the fitted J-R curves for all SE(B) specimens. Additionally, the blunting line, the 0.2 mm offset line, and the Δa max lines were also plotted.

3.3.3. Fracture toughness

The fracture toughness (J_{Ic} values) of the AlSi10Mg alloy produced by DED and determined according to the ASTM E1820–20b standard [24] are reported in Table 4. In this table, the a_0/W ratio, the stable

crack extension predicted by the elastic unloading compliance method (Δa_{pred}), the physical stable crack extension (Δa_p), and the difference among these values as a function of b_o (original remaining ligament) are also reported.

3.4. Fractographic analysis

3.4.1. Tensile test specimens

The fracture surfaces of the tensile specimens were analyzed with SEM and micrographs are reported in Fig. 11. Dimples on the investigated fracture surfaces are noticeable among the coarser pores, indicating the occurrence of a ductile fracture micro-mechanism. Secondary cracks originated from the pores, which act as stress concentrators, are also visible in both images (high magnification in Fig. 11-b).
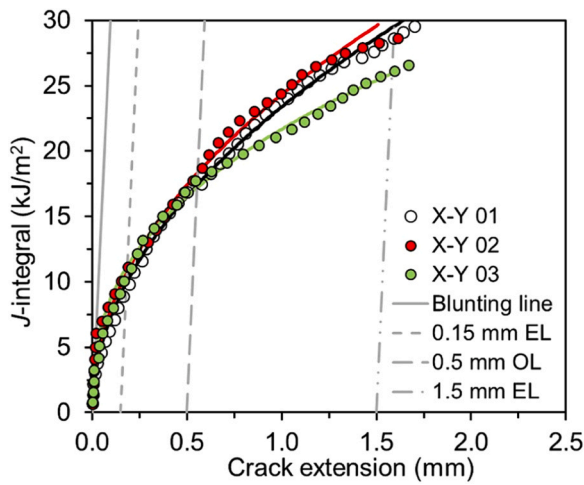
Fig. 7. J-Δa pairs of points of the X-Y SE(B) specimens.
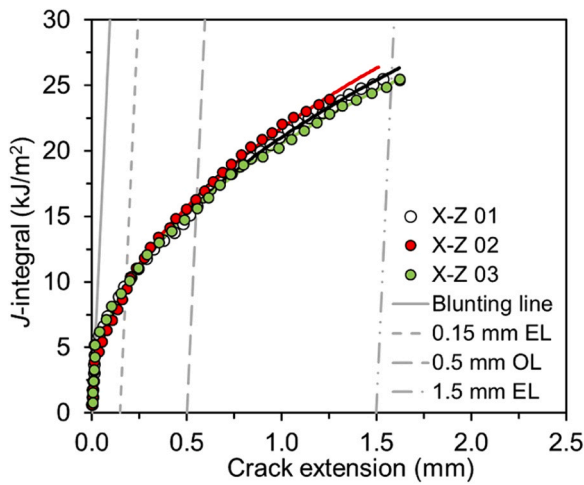
Fig. 8. J-Δa pairs of points of the X-Z SE(B) specimens.
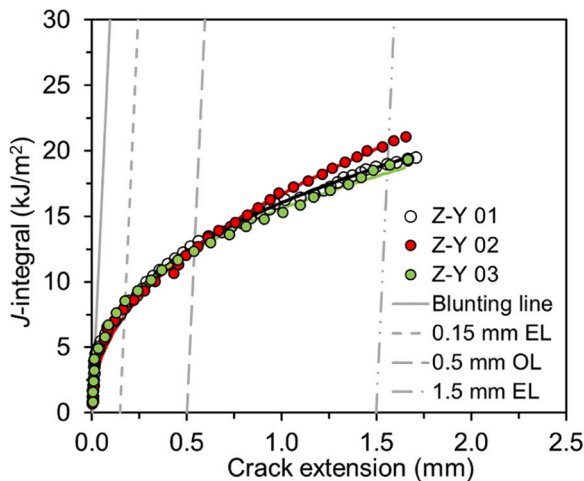
Fig. 9. J-Δa pairs of points for the Z-Y SE(B) specimens.

3.4.2. Fracture surfaces of SE(B) specimens and crack paths

The stable crack growth region of a representative SE(B) specimen per each crack plane orientation was investigated by SEM. Fig. 12 shows the stable crack growth region of specimens with the crack in the X-Y orientation. Fig. 13, for the crack in the X-Z, and Fig. 14, Z-Y orientation.

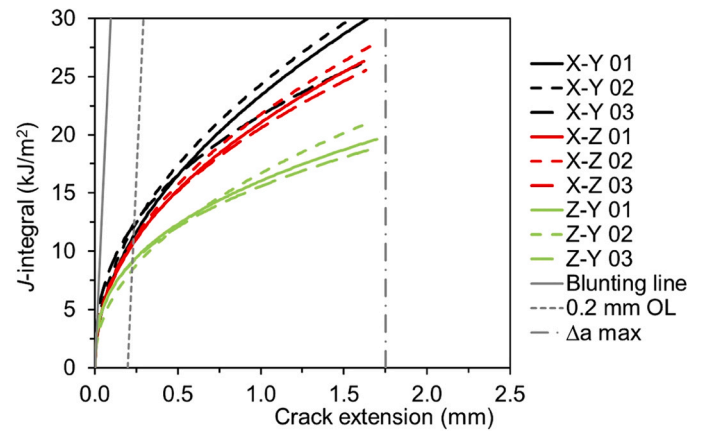The mid-sections perpendicular to the crack plane of representative

Fig. 10. Fitted *J*-R curves of the three crack plane orientations.

Table 4
Experimental fracture toughness for the AlSi10Mg alloy produced by DED.

Orientation	Specimen	J_{Ic} (kJ/m^2)	a_0/W	Δa_{pred} (mm)	Δa_p (mm)	Diff.
X-Y	01	11.32	0.49	1.70	1.88	0.03b_o
	02	12.18	0.50	1.71	1.99	0.04b_o
	03	12.37	0.49	1.81	2.03	0.03b_o
	Mean	11.96 ± 0.56	-	-	-	-
X-Z	01	10.65	0.52	1.62	1.84	0.03b_o
	02	11.02	0.50	1.68	1.90	0.03b_o
	03	10.82	0.49	1.65	1.97	0.04b_o
	Mean	10.83 ± 0.19	-	-	-	-
Z-Y	01	9.16	0.52	1.71	1.97	0.04b_o
	02	8.43	0.50	1.68	2.12	0.06b_o
	03	9.15	0.49	1.68	1.88	0.03b_o
	Mean	8.91 ± 0.42	-	-	-	-

fracture specimens for each crack plane orientation were also investigated by LOM, focusing on the pre-crack and stable crack growth regions. Fig. 15 shows the crack path of a specimen with an X-Y crack orientation at different magnifications. The path of a crack in the X-Z orientation is shown in Fig. 16, while in Fig. 17 the path of a specimen with the crack in the Z-Y.

Fig. 18 shows SEM images with high magnifications of the mid-sections perpendicular to the crack plane of representative SE(B) specimens for each crack plane orientation, showing the stable crack growth regions.

4. Discussion

From the results collected in Table 3, it can be observed that the AlSi10Mg alloy produced by DED and stress relieved features significant strain hardening, with the average σ_{UTS} value approximately twice the average value of σ_{YS}. Additionally, the tension test specimens feature limited necking before fracture. The σ_{YS} and σ_{UTS} values of AlSi10Mg determined in this work are lower than those achieved in previous works on the same alloy produced by DED, with σ_{UTS} showing the highest decrease (Table 5). These differences are mainly due to the different conditions in which the alloy was tested, i.e., as built and T6 for the literature works and stress relieved for this work. Different microstructural features and porosity levels due to the different printing setup and processing parameters might have also an effect on the mechanical properties of the material [28,29]. The lower resistance of the AlSi10Mg of this work with respect to the mechanical properties reported in Ref. [2,30] are consistent with previous work on the same alloy produced by LPBF. Amir et al. reported that for an AlSi10Mg alloy printed
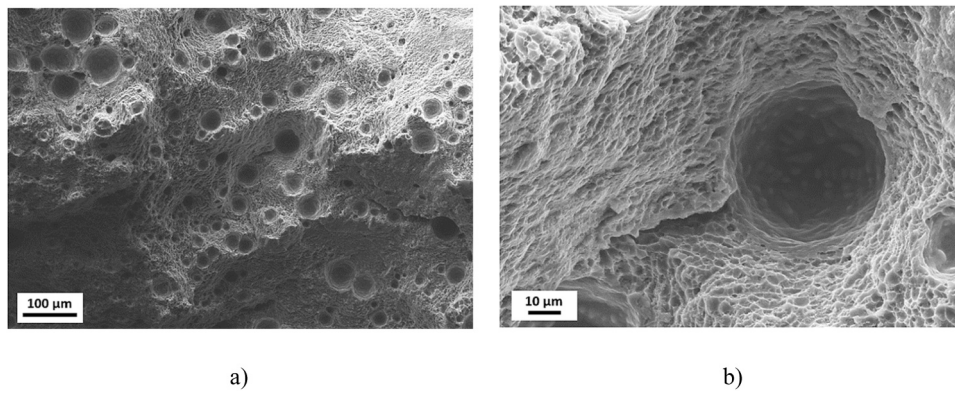
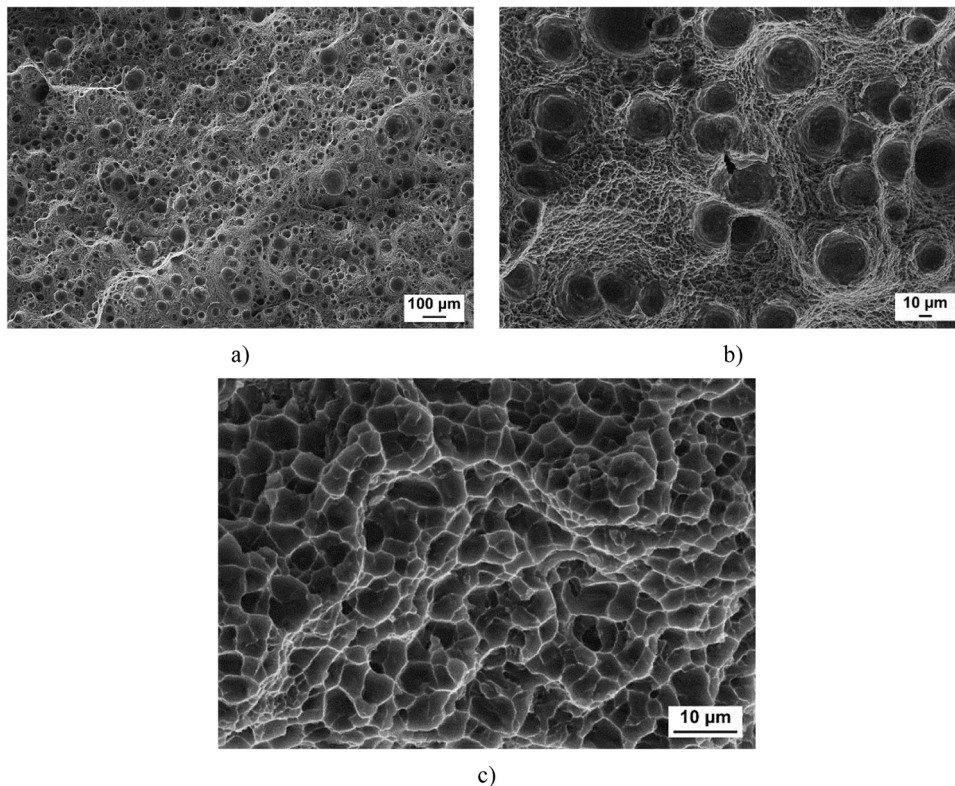**Fig. 11.** SEM images of the fracture surface of a representative tensile specimen at two magnifications: a) 500×, b) 3000×.

Fig. 12. Morphology of the stable crack growth region of a X-Y specimen at different magnification levels: a) 200 ×, b) 1000×, and c) 5000×.

with LPBF, the stress relieved heat treatment led to a worsening of the tensile performance with respect to the same material in as built condition. This behavior was associated to a reduction of the strength contribution given by the solid solution, to a coarsening of the eutectic Si particles, and to the increased distance among the Si particles [31,32]. Vice versa, the stress relief heat treatment has a beneficial effect on the elongation at fracture of the material [33].

The σ_{UTS} of AlSi10Mg processed by LPBF and stress relieved ranges from 220 to 360 MPa, the σ_{YS} between 170 and 225 MPa, and the elongation at fracture from 7.2% to 19.9% [33–37]. The tensile properties of the DED processed materials are lower with respect to the same material processed with LPBF. Such differences are due to the finer microstructural features that can be achieved by LPBF [38–40].

In Fig. 15 to Fig. 17, the LOM images of the mid-sections perpendicular to the crack planes are reported, showing the regions corresponding to the notch, the fatigue pre-crack, the stable crack growth, and the fatigue post-crack. It can be observed, for the X-Y specimens, that cracks did not follow a preferential path. On the other hand, cracks

in the Z-Y specimens follow the MPBs, which are favorably oriented along the crack plane. X-Z specimens show an intermediate behavior, with cracks that propagate through the pool cores, and, when favorable, they change their direction following the MPBs. From LOM images (Fig. 2) it is possible to notice that the microstructure at MPBs is not homogenous. Indeed, the melt pool boundaries include a heat-affected zone where a coarse microstructure is present. Pores are also visible in the aluminum matrix. LOM images in Fig. 2-a, Fig. 16 and Fig. 17 show that pores become more frequent close to the MPBs. Such discontinuities (i.e., pores and MPBs) is believed to play a fundamental role in governing the crack path and fracture toughness of the material. In addition, Fig. 15 to Fig. 17 also show that the fatigue pre-cracks start at the notch tips and follow smooth and almost straight paths, while within the stable crack growth region, the crack path is tortuous, following preferentially the pool boundaries and the pores. This discussion is schematically represented in Fig. 19, in which cracks are represented by the red lines, arrows indicate the crack growth orientation, and black spots represent the pores. The solidification microstructure composed of small dendrites
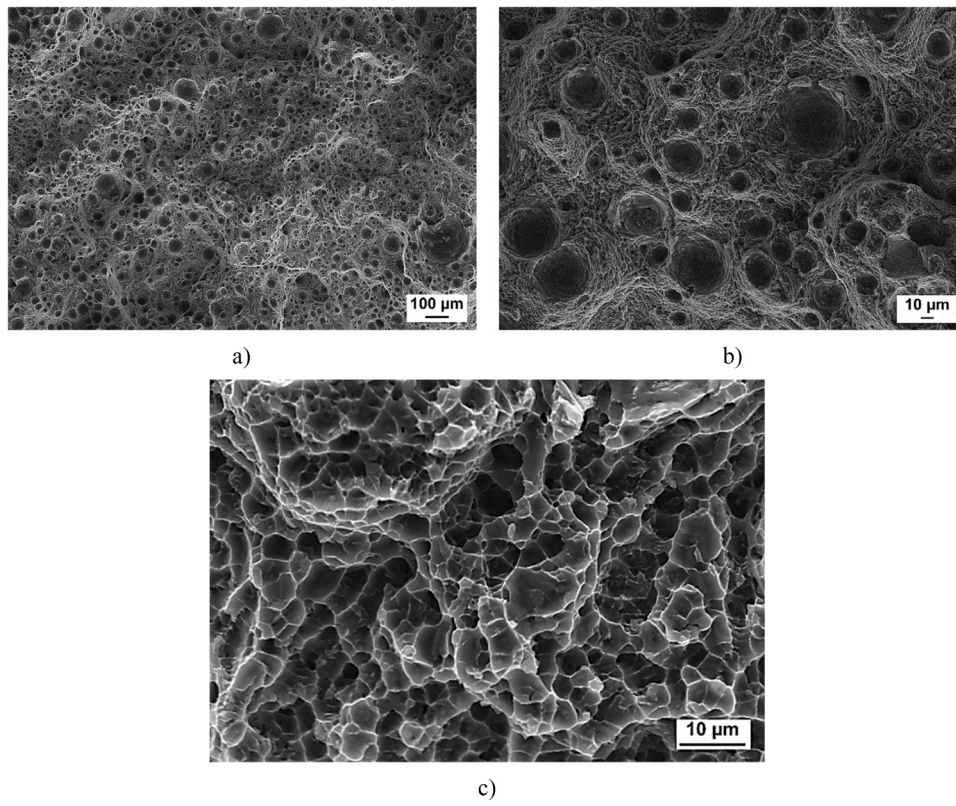
Fig. 13. Morphology of the stable crack growth region of a X-Z specimen at different magnification levels: a) 200 × , b) 1000×, and c) 5000×.
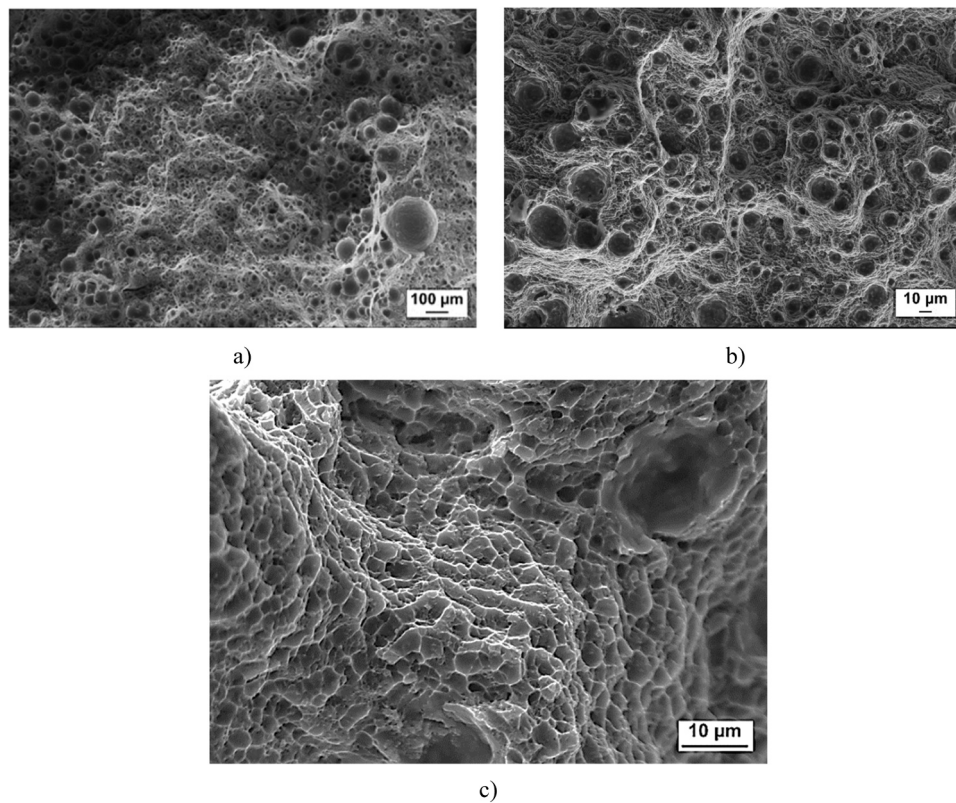

Fig. 14. Morphology of the stable crack growth region of a Z-Y specimen at different magnification levels: a) 200 × , b) 1000×, and c) 5000×.
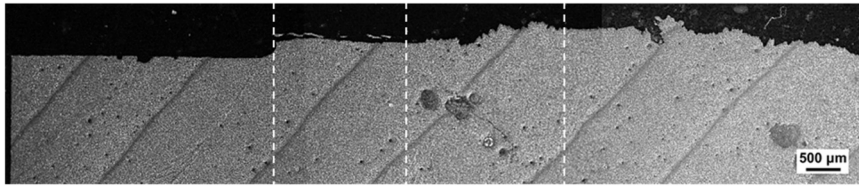
Fig. 15. LOM image of the crack profile of a X-Y specimen. From left to right: notch, fatigue pre-crack, stable crack growth, and fatigue post-crack regions.
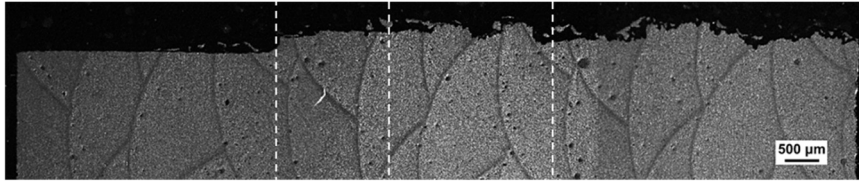

Fig. 16. LOM image of the crack profile of the X-Z SE(B) specimen. From left to right: notch, fatigue pre-crack, stable crack growth, and fatigue post-crack regions.
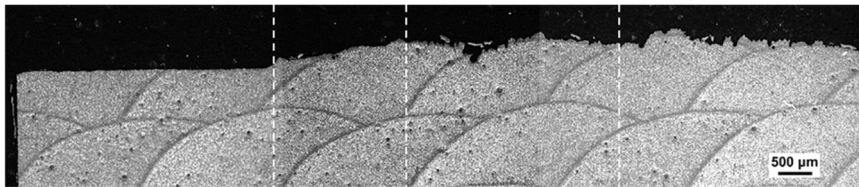

Fig. 17. LOM image of the crack profile of the Z-Y SE(B) specimen. From left to right: notch, fatigue pre-crack, stable crack growth, and fatigue post-crack regions.
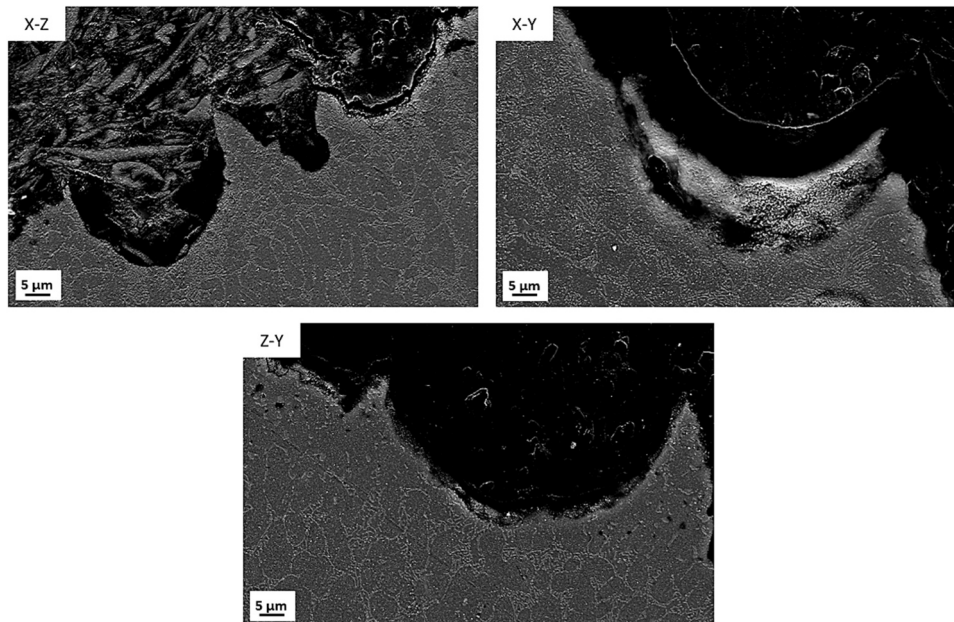

Fig. 18. SEM images from the mid-sections perpendicular to the crack plane in the stable crack growth regions of representative SE(B) specimens for each crack plane orientation.

Table 5
Average tensile properties of the AlSi10Mg alloy processed by DED according to this work and open literature.

	This work	Kiani *et al.* [2]	Zhou *et al.* [30]	Lv *et al.* [7]
Heat treatment	Stress relief	As built	As built	T6
σ_{UTS} (MPa)	209	344	317	342
σ_{YS} (MPa)	107	200	161	296
Elongation at break (%)	6.8	5.0	5.48	-

(Fig. 18) seems playing a minor role on the propagation of the fracture surface. In fact, cracks randomly propagate through the Al cell, without finding a preferential path along the intercellular/inter-dendritic regions in all the considered notch configurations. However, it has been reported in literature that, due to the stress relief heat treatment, the coarsening of the Si particles occurs. It was observed that a higher density of Si particles is found between the melt pool boundaries with respect to the core of the melt pools, where the Si particles are also smaller. This variation in the microstructure influences the mechanical properties of the material [41]. In particular, in the Z-Y samples, the
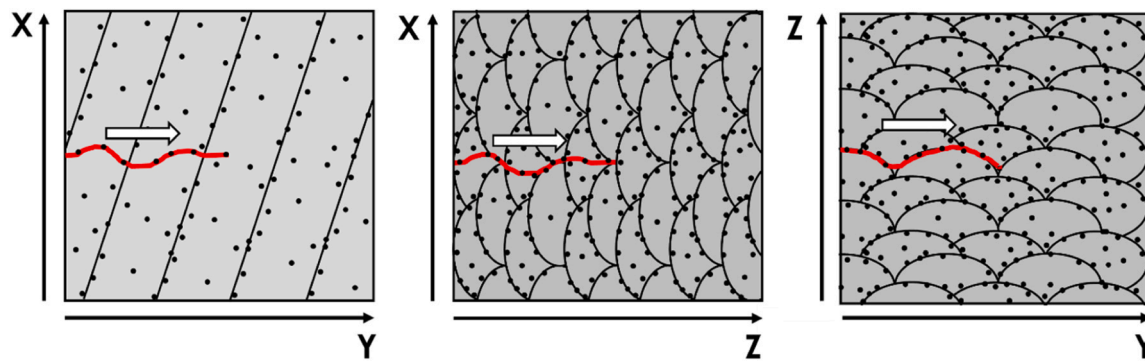
Fig. 19. Schematic representation of the crack propagation paths. The arrows indicate the crack propagation orientation in the three analyzed crack plane orientations (X-Y, X-Z and Z-Y, respectively).

crack propagates through melt pool boundaries where the density and size of the brittle Si phase are higher, thus further reducing the fracture toughness in this direction.

The fracture toughness values are consistent to what observed and described above regarding the crack paths. Indeed, the sample X-Y shows the highest fracture toughness value ($J_{Ic} = 11.96$ kJ/m^2), followed by the sample X-Z ($J_{Ic} = 10.83$ kJ/m^2) and by the sample Z-Y ($J_{Ic} = 8.91$ kJ/m^2). Such results are coherent to those achieved in a previous works on the fracture toughness of AlSi10Mg produced by LPBF, where it has been demonstrated that the lowest levels of fracture toughness are associated with cracks in the Z-Y orientation [11,42–48].

As in the case of tensile tests, the results of this study were compared to results available in literature on the same alloy but produced with LPBF. Araújo et al. studied fracture toughness properties of AlSi10Mg alloy processed by LPBF and stress relieved for different orientations. In X-Z direction J_{Ic} was equal to 11.4 kJ/m^2, while in Z-Y direction was equal to 10.4 kJ/m^2 [45]. By comparing such results with the results of this study, it can be claimed that DED samples show similar but slightly lower values of J_{Ic} than the same material printed with LPBF.

5. Concluding remarks

In this study, the tensile and fracture properties of AlSi10Mg parts produced by the DED technique and heat-treated were determined and analyzed. Regarding the tensile properties, the material showed average σ_{YS}, σ_{UTS}, and elongation at fracture values of 106 MPa, 208 MPa and 6.8%, respectively. These stress limits are lower than those reported in the literature for samples of the same alloy produced by additive manufacturing, whereas the elongation at break is higher. This behavior could be associated with different microstructural features and porosity levels due to the different experimental setup and with the reduction in the solid solution strengthening due to the heat treatment.

Anisotropy in the fracture toughness was observed among the three investigated crack plane orientations. Specimens with cracks in the X-Y orientation exhibited the highest fracture toughness ($J_{Ic} = 11.96 \pm 0.56$ kJ/m^2). Specimens with cracks in the X-Z orientation featured intermediate toughness ($J_{Ic} = 10.83 \pm 0.19$ kJ/m^2) while specimens with cracks in the Z-Y orientation featured the lowest toughness ($J_{Ic} = 8.91 \pm 0.42$ kJ/m^2). According to the observations, this anisotropy was mainly influenced by the distribution of MPBs, which were the weakest part of the DED alloy. Indeed, at melt pool boundaries the coarsening of the microstructure occurs and there is higher Si content, leading to that area being less resistant to crack propagation. It was observed that the pores were mainly located near the melt pool boundaries, and cracks tended to follow them when they were favorably oriented along these boundaries. Consequently, the crack growth resistance of these samples was the lowest, as in the case of the Z-Y specimens.

CRediT authorship contribution statement

Giorgia Lupi: Formal analysis, Investigation, Data curation, Writing – original draft, Writing – review & editing. **João Teixeira Oliveira de Menezes**: Methodology, Formal analysis, Investigation, Data curation, Writing – original draft, Writing – review & editing. **Filippo Belelli**: Investigation, Methodology, Writing – review & editing. **Francesco Bruzzo**: Investigation, Methodology, Writing – review & editing. **Elena Lopez**: Supervision, Methodology. **Joerg Volpp**: Project administration, Funding acquisition, Methodology, Writing – review & editing. **Enrique Mariano Castrodeza**: Supervision, Formal analysis, Methodology, Project administration, Writing – review & editing. **Riccardo Casati**: Supervision, Funding acquisition, Formal analysis, Methodology, Project administration, Writing - review & editing.

Declaration of Competing Interest

The authors declare that they have no known competing financial interests or personal relationships that could have appeared to influence the work reported in this paper.

Data Availability

Data will be made available on request.

Acknowledgements

References

[1] D. Herzog, V. Seyda, E. Wycisk, C. Emmelmann, Additive manufacturing of metals, Acta Mater. vol. 117 (2016) 371–392, https://doi.org/10.1016/J.ACTAMAT.2016.07.019.

[2] P. Kiani, A.D. Dupuy, K. Ma, J.M. Schoenung, Directed energy deposition of AlSi10Mg: single track nonscalability and bulk properties, Mater. Des. vol. 194 (2020), https://doi.org/10.1016/J.MATDES.2020.108847.

[3] J.C. Li, X. Lin, N. Kang, J.L. Lu, Q.Z. Wang, W.D. Huang, Microstructure, tensile and wear properties of a novel graded Al matrix composite prepared by direct energy deposition, J. Alloy. Compd. vol. 826 (2020), 154077, https://doi.org/10.1016/J.JALLCOM.2020.154077.

[4] D. Svetlizky, B. Zhengb, A. Vyatskikhb, M. Dasa, S. Bosec, A. Bandyopadhyayc, J. M. Schoenungb, E.J. Laverniab, Laser-based directed energy deposition (DED-LB) of advanced materials, Mater. Sci. Eng.: A vol. 840 (2022), 142967, https://doi.org/10.1016/J.MSEA.2022.142967.

[5] D.G. Ahn, Directed energy deposition (DED) process: state of the art, Int. J. Precis. Eng. Manuf. -Green. Technol. 2021 8:2 vol. 8 (2) (2021) 703–742, https://doi.org/10.1007/S40684-020-00302-7.

[6] S.M. Yusuf, N. Gao, Influence of energy density on metallurgy and properties in metal additive manufacturing, Mater. Sci. Technol. vol. 33 (11) (2017) 1269–1289, https://doi.org/10.1080/02670836.2017.1289444.

[7] F. Lv, L. Shen, H. Liang, D. Xie, C. Wang, Z. Tian, Mechanical properties of AlSi10Mg alloy fabricated by laser melting deposition and improvements via heat treatment, Opt. (Stuttg.) vol. 179 (2019) 8–18, https://doi.org/10.1016/J.IJLEO.2018.10.112.

[8] R. Casati, M. Coduri, S. Checchia, M. Vedani, Insight into the effect of different thermal treatment routes on the microstructure of AlSi7Mg processed by laser powder bed fusion, Mater. Charact. vol. 172 (2021), 110881, https://doi.org/10.1016/J.MATCHAR.2021.110881.

[9] X. Larráyoz Izcara, A. Guirao Blank, F. Pyczak, P. Staron, S. Schumann, N. Huber, Characterization and modeling of the influence of artificial aging on the microstructural evolution of age-hardenable AlSi10Mg(Cu) aluminum alloys, Mater. Sci. Eng.: A vol. 610 (2014) 46–53, https://doi.org/10.1016/J.MSEA.2014.04.031.

[10] L. Zhao, L. Song, J.G.S. Macías, Y. Zhu, M. Huang, A. Simar, Z. Li, Review on the correlation between microstructure and mechanical performance for laser powder bed fusion AlSi10Mg, Addit. Manuf. vol. 56 (2022), 102914, https://doi.org/10.1016/J.ADDMA.2022.102914.

[11] J.T. Oliveira de Menezes, E.M. Castrodeza, R. Casati, Effect of build orientation on fracture and tensile behavior of A357 Al alloy processed by Selective Laser Melting, Mater. Sci. Eng. A vol. 766 (2019), https://doi.org/10.1016/j.msea.2019.138392.

[12] L. Hitzler, E. Sert, A. Öchsner, E. Werner, Microstructure and mechanical property correlation for additively manufactured aluminum-silicon alloys, Qual. Anal. Addit. Manuf. Met.: Simul. Approaches, Process., Microstruct. Prop. (2023) 355–387, https://doi.org/10.1007/978-0-323-88664-2.00010-5.

[13] L. Hitzler, J. Hirsch, J. Schanz, B. Heine, M. Merkel, W. Hall, A. Öchsner, Fracture toughness of selective laser melted AlSi10Mg, Proc. Inst. Mech. Eng., Part L: J. Mater.: Des. Appl. vol. 233 (4) (2019) 615–621, https://doi.org/10.1177/1464420716687337/ASSET/IMAGES/LARGE/10.1177_1464420716687337-FIG5.JPEG.

[14] L. Hitzler, E. Sert, E. Schuch, A. Öchsner, M. Merkel, B. Heine, E. Werner, Fracture toughness of L-PBF fabricated aluminium–silicon: a quantitative study on the role of crack growth direction with respect to layering, Prog. Addit. Manuf. vol. 5 (3) (2020) 259–266, https://doi.org/10.1007/S40964-020-00113-X/TABLES/5.

[15] X. Wang, L. Li, J. Qu, W. Tao, Materials science and technology microstructure and mechanical properties of laser metal deposited AlSi10Mg alloys Microstructure and mechanical properties of laser metal deposited AlSi10Mg alloys, Mater. Sci. Technol. vol. 35 (18) (2019) 2284–2293, https://doi.org/10.1080/02670836.2019.1674022.

[16] B. Chen, Y. Yao, X. Song, C. Tan, L. Cao, J. Feng, "Microstructure and mechanical properties of additive manufacturing AlSi10Mg alloy using direct metal deposition," *https://doi.org/10.1080/00150193.2018.1392147*, vol. 523, no. 1, pp. 153–166, Jan. 2018, doi: 10.1080/00150193.2018.1392147.

[17] J. Gong, K. Wei, M. Liu, W. Song, X. Li, X. Zeng, Microstructure and mechanical properties of AlSi10Mg alloy built by laser powder bed fusion/direct energy deposition hybrid laser additive manufacturing, Addit. Manuf. vol. 59 (2022), 103160, https://doi.org/10.1016/J.ADDMA.2022.103160.

[18] C. Wei, H. Ye, Z. Zhao, J. Tang, X. Shen, G. Le, K. Ye, F. Le, Microstructure and fracture behavior of [90]W–[7]Ni-3Fe alloy fabricated by laser directed energy deposition, J. Alloy. Compd. vol. 865 (2021), 158975, https://doi.org/10.1016/J.JALLCOM.2021.158975.

[19] X. Yu, X. Lin, F. Liu, L. Wang, Y. Tang, J. Li, S. Zhang, W. Huang, Influence of post-heat-treatment on the microstructure and fracture toughness properties of Inconel 718 fabricated with laser directed energy deposition additive manufacturing, Mater. Sci. Eng. A vol. 798 (2020), https://doi.org/10.1016/J.MSEA.2020.140092.

[20] S. Shrestha, J. el Rassi, M. Kannan, G. Morscher, A.L. Gyekenyesi, O.E. Scott-Emuakpor, Fracture toughness and fatigue crack growth rate properties of AM repaired Ti–6Al–4V by direct energy deposition, Mater. Sci. Eng.: A vol. 823 (2021), 141701, https://doi.org/10.1016/J.MSEA.2021.141701.

[21] S.A. Ojo, S. Shrestha, J. El Rassi, R.P. Panakarajupally, K. Manigandan, G. N. Morscher, A.L. Gyekenyesi, O.E. Scott-Emuakpor, The use of compact specimens to determine fracture toughness anisotropy of Ti–6Al–4V additively manufactured for repair, Mater. Sci. Eng.: A vol. 823 (2021), 141779, https://doi.org/10.1016/J.MSEA.2021.141779.

[22] A. Da Silva, F. Belelli, G. Lupi, F. Bruzzo, B. Brandau, L. Maier, A. Pesl, J. Frostevarg, R. Casati, E. Lopez, A.F.H. Kaplan, Influence of aluminium powder aging on directed energy deposition, Mater. Des. vol. 218 (2022), https://doi.org/10.1016/J.MATDES.2022.110677.

[23] "ASTM E8 / E8M-13a, Standard Test Methods for Tension Testing of Metallic Materials, ASTM International, West Conshohocken, PA, 2013", [Online]. Available: ⟨www.astm.org⟩,

[24] "ASTM E1820–20b, Standard Test Method for Measurement of Fracture Toughness, ASTM International, West Conshohocken, PA, 2020", [Online]. Available: ⟨www.astm.org⟩.

[25] "ISO/ASTM 52921:2013 Standard terminology for additive manufacturing — Coordinate systems and test methodologies, ASTM International, West Conshohocken, PA,2013", [Online]. Available: ⟨www.astm.org⟩.

[26] British Standards Institution, Fract. Mech. toughness Test. Pt. 1 Method Determ. KIc, Crit. CTOD Crit. J. Values Met. Mater. BSI (1991).

[27] A. Sola, A. Nouri, Microstructural porosity in additive manufacturing: the formation and detection of pores in metal parts fabricated by powder bed fusion,

[28] J. Turicek, S.P. Patil, B. Marker, Effects of porosity on the mechanical properties of additively manufactured components: a critical review, Mater. Res Express vol. 7 (12) (2020), 122001, https://doi.org/10.1088/2053-1591/ABCC5D.

[29] M.C. Brennan, J.S. Keist, T.A. Palmer, Defects in metal additive manufacturing processes, J. Mater. Eng. Perform. 2021 30:7 vol. 30 (7) (2021) 4808–4818, https://doi.org/10.1007/S11665-021-05919-6.

[30] J. Zhou, X. Zhou, H. Li, J. Hu, X. Han, S. Liu, In-situ laser shock peening for improved surface quality and mechanical properties of laser-directed energy-deposited AlSi10Mg alloy, Addit. Manuf. vol. 60 (2022), 103177, https://doi.org/10.1016/J.ADDMA.2022.103177.

[31] B. Amir, E. Grinberg, Y. Gale, O. Sadot, S. Samuha, Influences of platform heating and post-processing stress relief treatment on the mechanical properties and microstructure of selective-laser-melted AlSi10Mg alloys, Mater. Sci. Eng.: A vol. 822 (2021), 141612, https://doi.org/10.1016/J.MSEA.2021.141612.

[32] J. Fiocchi, A. Tuissi, P. Bassani, C.A. Biffi, Low temperature annealing dedicated to AlSi10Mg selective laser melting products, J. Alloy. Compd. vol. 695 (2017) 3402–3409, https://doi.org/10.1016/J.JALLCOM.2016.12.019.

[33] Mfusi, Mathe, Tshabalala, Popoola, The effect of stress relief on the mechanical and fatigue properties of additively manufactured AlSi10Mg Parts, Metals vol. 9 (11) (2019) 1216, https://doi.org/10.3390/met9111216.

[34] E. Padovano, C. Badini, A. Pantarelli, F. Gili, F. D'Aiuto, A comparative study of the effects of thermal treatments on AlSi10Mg produced by laser powder bed fusion, J. Alloy. Compd. vol. 831 (2020), 154822, https://doi.org/10.1016/J.JALLCOM.2020.154822.

[35] A. Iturrioz, E. Gil, M.M. Petite, F. Garciandia, A.M. Mancisidor, M. San Sebastian, Selective laser melting of AlSi10Mg alloy: influence of heat treatment condition on mechanical properties and microstructure, Weld. World vol. 62 (4) (2018) 885–892, https://doi.org/10.1007/s40194-018-0592-8.

[36] N.E. Uzan, R. Shneck, O. Yeheskel, N. Frage, High-temperature mechanical properties of AlSi10Mg specimens fabricated by additive manufacturing using selective laser melting technologies (AM-SLM), Addit. Manuf. vol. 24 (2018) 257–263, https://doi.org/10.1016/J.ADDMA.2018.09.033.

[37] W.J. Hwang, G.B. Bang, S.H. Choa, Effect of a stress relief heat treatment of AlSi7Mg and AlSi10Mg alloys on mechanical and electrical properties according to silicon precipitation, Met. Mater. Int. vol. 29 (5) (2022) 1311–1322, https://doi.org/10.1007/S12540-022-01304-7/TABLES/4.

[38] N. Martin, A. Hor, E. Copin, P. Lours, L. Ratsifandrihana, Correlation between microstructure heterogeneity and multi-scale mechanical behavior of hybrid LPBF-DED Inconel 625, J. Mater. Process Technol. vol. 303 (2022), 117542, https://doi.org/10.1016/J.JMATPROTEC.2022.117542.

[39] M. Godec, S. Malej, D. Feizpour, Č. Donik, M. Balažic, D. Klobčar, L. Pambaguian, M. Conradi, A. Kocijan, Hybrid additive manufacturing of Inconel 718 for future space applications, Mater. Charact. vol. 172 (2021), 110842, https://doi.org/10.1016/J.MATCHAR.2020.110842.

[40] L. Li, T. Yuan, B. Feng, The microstructures and mechanical properties of Al-Zn-Mg-Cu-Si-Zr alloy: a comparison between directed energy deposition and laser powder bed fusion, Mater. Lett. vol. 337 (2023), 133959, https://doi.org/10.1016/J.MATLET.2023.133959.

[41] K.G. Prashanth, S. Scudino, H.J. Klauss, K.B. Surreddi, L. Löber, Z. Wang, A. K. Chaubey, U. Kühn, J. Eckert, Microstructure and mechanical properties of Al–12Si produced by selective laser melting: effect of heat treatment, Mater. Sci. Eng.: A vol. 590 (2014) 153–160, https://doi.org/10.1016/J.MSEA.2013.10.023.

[42] L. Hitzler, J. Hirsch, J. Schanz, B. Heine, M. Merkel, W. Hall, A. Öchsner, Fracture toughness of selective laser melted AlSi10Mg vol. 233 (4) (2017) 615–621, https://doi.org/10.1177/1464420716687337. ⟨https://doi.org/10.1177/1464420716687337,⟩.

[43] S. AlRedha, A. Shterenlikht, M. Mostafavi, D. Van Gelderen, O.E. Lopez-Botello, L. A. Reyes, P. Zambrano, C. Garza, Effect of build orientation on fracture behaviour of AlSi10Mg produced by selective laser melting, Rapid Prototyp. J. vol. 27 (1) (2021) 112–119, https://doi.org/10.1108/RPJ-02-2020-0041.

[44] Z.W. Xu, A. Liu, X.S. Wang, The influence of building direction on the fatigue crack propagation behavior of Ti6Al4V alloy produced by selective laser melting, Mater. Sci. Eng. A vol. 767 (2019), https://doi.org/10.1016/J.MSEA.2019.138409.

[45] L.C. Araújo, A.H. Gabriel, E.B. da Fonseca, J.A. Avila, A.L. Jardini, R.S. Junior, É. S. Lopes, Effects of build orientation and heat treatments on the tensile and fracture toughness properties of additively manufactured AlSi10Mg, Int J. Mech. Sci. vol. 213 (2022), 106868, https://doi.org/10.1016/J.IJMECSCI.2021.106868.

[46] M.J. Paul, Q. Liu, J.P. Best, X. Li, J.J. Kruzic, U. Ramamurty, B. Gludovatz, Fracture resistance of AlSi10Mg fabricated by laser powder bed fusion, Acta Mater. vol. 211 (. 2021), 116869, https://doi.org/10.1016/J.ACTAMAT.2021.116869.

[47] Q. Liu, H. Wu, M.J. Paul, P. He, Z. Peng, B. Gludovatz, J.J. Kruzic, C.H. Wang, X. Li, Machine-learning assisted laser powder bed fusion process optimization for AlSi10Mg: New microstructure description indices and fracture mechanisms, Acta Mater. vol. 201 (2020) 316–328, https://doi.org/10.1016/J.ACTAMAT.2020.10.010.

[48] I. Rosenthal, A. Stern, N. Frage, Strain rate sensitivity and fracture mechanism of AlSi10Mg parts produced by selective laser melting, Mater. Sci. Eng.: A vol. 682 (2017) 509–517, https://doi.org/10.1016/J.MSEA.2016.11.070.

J. Adv. Manuf. Process vol. 1 (3) (2019), e10021, https://doi.org/10.1002/AMP2.10021.